

Characterisation of the luminescence properties of BAM:Eu²⁺ particles as a tracer for thermographic particle image velocimetry

Benoit Fond¹ · Christopher Abram² · Frank Beyrau²

Received: 22 May 2015 / Accepted: 28 October 2015 / Published online: 23 November 2015
© The Author(s) 2015. This article is published with open access at Springerlink.com

Abstract Thermographic phosphor particles are seeded into the flow as tracers for simultaneous temperature and velocity measurements in fluids. Several studies using different phosphors as gas-phase tracers have been published in recent years. However, little is known about their emission characteristics when they are dispersed as individual particles in the fluid. In this paper, the luminescence properties of BAM:Eu²⁺ particles, a phosphor with favourable characteristics (short luminescence lifetime, blue emission spectrum, high quantum efficiency), are thoroughly investigated in the gas phase. Using a recently developed particle-counting tool, the emission intensity per particle is measured over a wide range of conditions, including for various temperatures from 300 to 920 K, in air and in pure nitrogen. The luminescence emission per particle is shown to drop with temperature, but to be insensitive to the seeding density and to the oxygen content over the tested range. Together with a spectroscopic study, and a statistical error analysis, these results are used to predict the temperature precision of the technique under various conditions for different filter combinations and to assess the current upper temperature limit of this phosphor for practical applications. Potential additional sources of uncertainty are also investigated, including cross-dependencies of the measured intensity ratio on the seeding density, excitation fluence and oxygen partial pressure in the gas phase. Only a weak

dependence on the laser fluence is observed, while the measured intensity ratio is shown to be insensitive to both seeding density and the oxygen volume fraction. Finally, the saturation behaviour of the phosphorescence emission is examined, through theoretical considerations and measurements performed with different excitation schemes in an attempt to increase signal levels. In conclusion, this paper confirms that BAM:Eu²⁺ is a very suitable tracer for measurements in turbulent flows up to 900 K.

1 Introduction

Optical measurement techniques have a huge impact on our understanding of complex turbulent flow phenomena. Techniques capable of simultaneously imaging velocity-scalar quantities are particularly beneficial, allowing, for example, the direct measurement of turbulent diffusion and providing invaluable insight into the interactions between the turbulent flow field and density fluctuations or reaction chemistry.

Recently, a novel technique for simultaneous temperature and velocity imaging has been developed. It is based on thermographic phosphors, which are solid materials with luminescence properties that can be used for remote temperature sensing. These particles are seeded into the flow under investigation. Using a conventional particle image velocimetry (PIV) approach, visible laser light scattered by the particles is recorded to determine the velocity field. Simultaneously, a UV laser is used to excite the particles, and their temperature-sensitive phosphorescence emission is recorded to determine the particle temperature applying a two-colour intensity ratio method. For micrometre-size particles, it can be shown that the particle temperature and velocity match that of the surrounding gas [1], with both

✉ Frank Beyrau
frank.beyrau@ovgu.de

¹ Department of Mechanical Engineering, Imperial College London, London SW7 2AZ, UK

² Lehrstuhl für Technische Thermodynamik, Otto-von-Guericke-Universität Magdeburg, 39106 Magdeburg, Germany

the temperature and velocity response times in the range of 10–100 μs for 2 μm spherical particles, depending on gas temperature and the physical properties of the particles.

The principle of this thermographic PIV technique has been demonstrated for time-averaged [2] and single-shot measurements [1, 3, 4] as well as at kHz rates for temporally resolved measurements [5]. A similar concept called thermographic laser Doppler velocimetry was also demonstrated for point-wise measurements with high spatial resolution using continuous wave lasers and photomultiplier tubes [6].

This concept is very attractive for several reasons. It requires relatively simple instrumentation in terms of lasers and cameras (solid-state lasers for excitation, and non-intensified cameras for detection), and a single tracer is seeded into the flow. Also, in contrast to gaseous tracers used for laser-induced fluorescence (LIF) thermometry (e.g. acetone, toluene), many thermographic phosphors are inert, have a high melting point (>1900 K) and are in general insensitive to pressure and to the gas composition, making them particularly suitable as a tracer for reacting flow applications.

In recent years, there have been several studies using thermographic phosphors for gas thermometry [1–13], and different phosphors have been used. Some important luminescence properties of these phosphors are indicated in Table 1.

The ideal luminescent tracer for gas-phase measurements has an excitation spectrum extending to the near UV region, to allow 355 nm excitation. An excitation wavelength deeper in the UV, e.g. 266 nm, is prone to cause unwanted fluorescence emission from chemical species potentially present in the flow. The absorption cross section and quantum efficiency of the phosphor are high to maximise the luminescence output, even at low excitation fluences. The spectral regions that the ratiometric response utilises are in the blue region, to allow an efficient detection with non-intensified cameras and simultaneously minimise interferences from Planck's radiation. Finally, when the camera exposure is limited by the flow timescales under

investigation, the choice of a phosphor with a short lifetime maximises the recorded signal.

The authors previously used BAM:Eu²⁺, a phosphor which shares many properties with the ideal phosphor described above. It has a broad excitation spectrum extending to the near UV, allowing 355 nm excitation. Its subsequent emission is fast (1 μs), in the blue region of the visible spectrum and has a high quantum yield (>90 % [16]). These factors suggest that BAM:Eu²⁺ is a promising phosphor, and indeed it has been successfully used for precise temperature measurements. It was even employed for measurements at kHz rate, using a diode-pumped solid-state laser, despite the low pulse energy (~1 mJ) offered by these lasers [5].

However, for all the phosphors in Table 1, and other phosphors which could prove suitable for gas temperature measurements, there are no quantitative studies on the luminescence of dispersed particles in the gas phase. This is in direct contrast with the well-understood physical processes of organic tracers used for flow measurements, see, e.g. the review article by Schulz and Sick [17], and so quantitative investigations are needed to compare different phosphors, predict signal levels for various practical applications and analyse any cross-dependencies of the measured temperature on other parameters such as the excitation fluence or seeding density.

Investigating phosphors in conditions close to those of practical measurements is a challenging task. As discussed in [14], investigations must be performed in the gas phase and not in aggregated powder form where the effects of multiple scattering dominates and where the particles probed are subjected to a repeated illumination, which could accentuate particle heating and/or lead to damage. However, because it is difficult to set, control and reproduce seeding conditions in the gas phase, the number density of particles must be measured in situ in order to determine the emission characteristics of phosphor particles on a per-particle basis. In our previous work [14], a particle-counting system was developed and demonstrated, allowing the simultaneous measurement of seeding density and

Table 1 Phosphors used in gas-phase thermometry studies

Phosphor	Lifetime	Excitation wavelength (nm)	Spectral region used for thermometry (nm)	Studies
YAG:Dy ³⁺	1 ms	355	440–500	[7, 8, 12]
Mg ₄ FGeO ₆ :Mn ⁴⁺	3 ms	355	600–700	[2, 4]
Y ₂ O ₂ S:Er ³⁺ , Yb ³⁺	50 μs	980 ^a	510–570	[9]
YAG:Pr ³⁺	190 μs ^b	266	470–640	[3, 10]
BAM:Eu ²⁺	1 μs	355	380–500	[1, 5, 6, 11, 12, 14]
ZnO	<1 ns	355	370–430	[13]

^a Y₂O₂S:Er³⁺, Yb³⁺ is an up-conversion phosphor

^b Lifetime of the ¹D₂ → ³H₄ emission at around 610 nm used in the ratio evaluation, taken from [15]

signal level for various conditions. By correcting for variations of seeding density, the influence of other parameters on the collected phosphorescence intensity can be isolated.

In this paper, the luminescence properties of BAM:Eu²⁺ tracer particles are thoroughly investigated in the gas phase. Following a description of the experimental method (Sect. 2), and of the theoretical models used in these studies (Sect. 3), the emission intensity is characterised on a per-particle basis over a wide range of conditions (Sect. 4.1), including various temperatures up to 920 K, different bath gases (air and nitrogen) and excitation fluences. Based on these results, and on emission spectra recorded at various temperatures, predictions of the achievable temperature precision are then performed for several filter combinations in order to determine the upper temperature range of this phosphor (Sect. 4.2). Possible sources of uncertainty are also investigated (Sect. 4.3). These may originate from cross-dependencies of the measured intensity ratio (and in consequence the measured temperature) on the seeding density, the excitation fluence or the oxygen concentration. The last part of this paper (Sect. 4.4) explores possible causes for the saturation behaviour of the phosphorescence emission with laser fluence in an attempt to improve signal levels. Results obtained using different excitation schemes are presented.

2 Experimental set-up

2.1 Phosphor particles and test cases

BAM:Eu²⁺ thermographic phosphor particles (KEMK63/UF-P1, Phosphor Technology, median diameter (based on volume): 2.4 μm , median diameter (based on number): 1 μm , sizing technique: Counter Coulter) were used as a tracer. The authors previously showed that such particles, were they spherical, accurately trace the gas temperature and the flow velocity [1] in most turbulent flows of interest. A scanning electron microscope image of the particles is presented on Fig. 1 clearly showing that the particles are non-spherical. Their parallelepiped shape can be expected to offer improved tracing abilities in comparison with spheres of the same projected diameter. Prior to use, a SiO₂ nanoparticle coating (Ludox[®]) was applied to reduce inter-particle forces by cancelling surface charges, and the powder was dried for 8 h in a furnace at 125 °C to remove any moisture.

The particles were seeded into the various gas streams using a custom-built reverse cyclone seeder. The seeding density was adjusted by controlling the air velocity in the seeder, which was achieved by changing the pressure drop in a stream that bypassed the seeder.

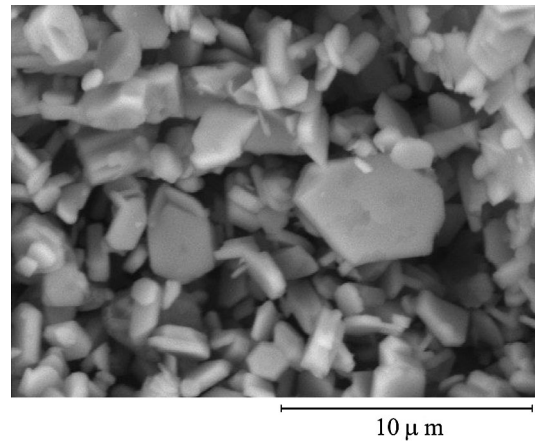


Fig. 1 Scanning electron microscopic image of BAM:Eu²⁺ particles (KEMK63/UF-P1). Courtesy of Phosphor Technology Ltd

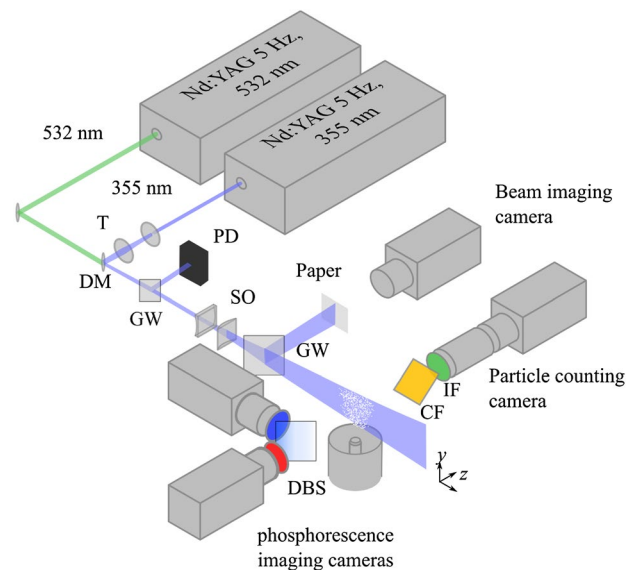


Fig. 2 Experimental set-up. *T* telescope, *DM* dichroic mirror, *SO* sheet optics, *GW* glass window, *PD* photodiode, *IF* interference filter, *CF* coloured glass filter, *DBS* plate dichroic beam splitter

For the room-temperature studies, a 40 mm diameter jet of air was used. For higher temperatures, the seeded stream flowed through an 8 mm inside-diameter, 2.5 m-long stainless steel coil placed inside a high-temperature oven. The temperature of the jet was measured using a fine 50 μm diameter type K thermocouple. With this system, it is possible to obtain jet exit temperatures of up to 1200 K. Finally, to investigate possible effects of oxygen quenching on the phosphorescence emission, this rig was alternately supplied with air and pure nitrogen.

2.2 Phosphorescence excitation and detection

Unless otherwise specified, the phosphor particles were excited using the third harmonic of a 5 Hz pulsed Nd:YAG laser at 355 nm (Quanta-Ray GCR-150, Spectra-Physics), with a pulse duration of 7 ns. A 680 μm thick light sheet (see Sect. 2.5) was formed in the measurement plane (Fig. 2).

The phosphorescence emission from the particles was detected by two hardware-binned (4×4) non-intensified interline transfer CCD cameras (Imager Intense, LaVision, 1376×1040 pixels, 6.45 μm pixel size) with 50 mm f/1.4 Nikon lenses. Two high-transmission-interference (>80 %) filters at 440-90 and 464-40 nm and a 455 nm long-pass dichroic plate beam splitter, AR-coated on the reverse side, were used to exploit the temperature-dependent shift and broadening of the emission line for the ratio-based temperature measurement (see Ref. [1]). The camera/beam splitter system was carefully adjusted using micrometre stages to minimise relative distortion and differences in light collection path. The camera exposure time was set to 5 μs , beginning 1 μs before the excitation laser pulse. The field of view of the cameras was 28×21 mm.

Interline transfer CCDs can achieve exposure times down to 1 μs with acceptable level of jitter, obviating the need for the fast gating offered by image intensifiers, which are associated with nonlinearity and higher noise levels. To improve further the detector sensitivity in applications when long (~ms) exposure times are permitted, an EMCCD can also be used. However, in highly luminous flames, even an interline transfer CCD cameras may not avoid contributions from chemiluminescence or blackbody radiation from hot particles, and intensified cameras may be required. Here, the CCD cameras were hardware-binned (4×4) to reduce the contribution of the read-out noise to the measurement.

The image recorded by a camera in the absence of incident light is called the dark image. The amplifiers of the cameras are adjusted in the factory to generate an offset, which ensures that the ADC converter only issues positive values. These components are temperature-sensitive, and so is the resulting offset. For the cameras used here, this offset is between 20 and 60 counts. However, even after the cameras were turned on and the indicated temperature reaches the set value of -12 $^{\circ}\text{C}$, drift in this offset was identified. It was also found that the camera offset can vary by 2–3 counts over a recording sequence, due to the absence of temperature regulation of the chip. Also, changes from Idle to Run lead to temperature differences, reflected in a continuous offset change over the first frames of a recording. Considering typical room-temperature measurement conditions, with a ratio of 0.4 and a pixel intensity of 200 counts

in the strongest channel, these variations would lead to a maximum of 3.5 % error in the measured intensity ratio (~17 K around room temperature).

In order to account for such variations, images were recorded at a rate twice as high as that of the laser, so that the laser only illuminated every second frame. This allows the evaluation of the camera offset between illuminated frames in order to adjust the background subtraction on a frame-to-frame basis. A time-averaged background image was compiled from all non-illuminated images. A factor was then applied for each image subtraction, which is the ratio of the instantaneous spatial average of the intensity of each non-illuminated image to the spatial average of the time-averaged background. Using this approach removes the effects of these fluctuations.

The background-subtracted images were then corrected for nonlinearity. The linearity response of the cameras was determined using a 3 inch diameter integrating sphere (Labsphere) and a photodiode DET10A (Thorlabs). The irradiance on the camera chip was varied using an aperture at the sphere entrance port, which was illuminated by the emission of a BAM:Eu²⁺ phosphor pellet following laser excitation at constant pulse energy. This arrangement covered a suitable range of irradiance on the chip during the short exposure time used in the actual measurements, and allowed for the dynamic background subtraction procedure described above. The uncertainty in the camera calibration was estimated to be ~3 % resulting from the uncertainty in the linearity of the detector (photodiode) monitoring the sphere radiance, and the uncertainty in the sphere uniformity.

To increase the signal-to-noise ratio and reduce the effect of residual displacement between the two images, a 7×7 moving average filter was applied to the images for a final resolution of 600 μm , as measured using a USAF resolution target, which also corresponds to the laser sheet thickness, therefore resulting in cubic elementary probe volumes. For measurements of absolute phosphorescence intensity, the recorded intensity in the one of the phosphorescence camera (equipped with the 464-40 nm filter) was averaged over a region that matches the field of view (8×6 mm²) of the counting camera (see Sect. 2.3 below).

Image pairs were divided, and resulting ratio images were themselves divided by an average ratio image obtained at room temperature to correct for non-uniformities in the light collection efficiency. No software mapping was applied before division of the images. When needed, the ratio images were converted to temperature using inflow calibration data obtained with the same detection system (camera and spectral filters).

2.3 Particle counting

The particle-counting system is identical to that described in [14]. Only a brief description is given here. The particles were illuminated with light from a frequency-doubled Nd:YAG laser operating at 5 Hz. Using a 355 nm long-pass dichroic mirror and a cylindrical lens (+750 mm), a thin light sheet (160 μm) was formed along the same optical path as the 355 nm light sheet. High-resolution particle images recorded using an interline transfer CCD camera (Imager Intense, LaVision, 1376 \times 1040 pixels, 6.45 μm pixel size) were then processed in MATLAB in order to evaluate the number of local maxima, which is used as a measure of the number of particles as described in [14].

2.4 Alternative excitation schemes

To investigate the influence of the laser wavelength and bandwidth on the phosphorescence emission, two additional sources were used.

A frequency-quadrupled 5 Hz Nd:YAG laser (Quanta-Ray Lab 150, Spectra-Physics) provided excitation at 266 nm, with a pulse duration of 7 ns and a spectral bandwidth of $<1\text{ cm}^{-1}$. Additionally, a dye laser was used to provide a broadband light source compared to the very narrowband Nd:YAG laser. The main amplifier cuvette of a dye laser (Narrowscan, Radiant Dyes) was filled with Exalite 376 (Exciton) and pumped by the frequency-tripled Nd:YAG laser. The cavity was formed without any bandwidth or frequency-selective elements, using a highly reflective broadband UV mirror and a one-side anti-reflective coated glass window as cavity and the 40 mm main amplifier cuvette as active medium. The spectrum of this laser output has a central wavelength of 376 nm and a bandwidth (FWHM) of about 200 cm^{-1} (3 nm), as measured using a spectrometer.

The 266 and 355 nm beams were overlapped in the measurement plane using 266 nm long-pass dichroic mirrors for the 355/266 nm comparison. For the broadband/narrowband comparison, a one-side-coated anti-reflective glass window was used to combine the 355 and 376 nm beams. Finally, cylindrical lenses and Galilean telescopes were used to form light sheets and control their thicknesses independently.

For both studies, quasi-simultaneous excitation was used so that the same particles were probed, alleviating the need for particle counting. The two laser pulses (e.g. 355 and 266 nm) were separated by 10 μs , which is larger than the luminescence lifetime of the phosphor (1 μs). The phosphorescence detection system was that described in Sect. 2.2, but with the same 10 μs delay between the camera exposures in order to separate the two subsequent luminescence signals. Each exposure was

set to 5 μs , beginning 1 μs before its respective excitation pulse.

2.5 Beam diagnostics

All sheets were reflected using a glass window with an AR coating on the reverse side onto a thin piece of paper positioned at the second, reflected focus of the light sheet. This paper was imaged onto a CCD camera equipped with an 85-mm Nikkor lens in order to monitor the sheet characteristics in the probe volume in situ, c.f. [18]. The resolution of the imaging system was determined using a USAF resolution target. The images of the sheets reflected from both the front and the back surface of the glass window were found to have the same FWHM thickness. This was true for all four wavelengths tested (266, 355, 376, 532 nm) confirming the homogeneity and linear character of the paper fluorescence. Although it is preferable for beam profiling to directly illuminate the camera with the attenuated beam, in particular to avoid photo-bleaching of the paper after repeated illumination, this approach would not allow imaging at 266 nm, which is outside the spectral range of the CCD camera.

2.6 Oven spectroscopy

The temperature sensitivity of the phosphorescence emission spectrum was assessed between 300 and 1100 K based on measurements performed on aggregated powder form, since particles in the gas phase would require excessive averaging for spectrally resolved measurements due to the relatively low signal levels. Our previous measurements reported in [1] were limited to 700 K because several studies had reported evidence of thermal degradation occurring in BAM:Eu²⁺ powder samples after extended (1-h) exposure to temperatures exceeding 770 K [19, 20]. Under these conditions, the oxidation state of the Eu²⁺ atoms increases to Eu³⁺, resulting in a sharp and permanent drop in the room-temperature emission intensity of the blue broadband phosphorescence. This degradation also results in a small redshift linked to an increase in the crystal field acting on the Eu²⁺ atoms due to the appearance of neighbouring Eu³⁺. For an exposure of an hour at 770 K in air, a shift of about 2 nm was reported [21]. It is unlikely that this degradation phenomenon will have an effect on temperature measurement in high-temperature flows, considering the much shorter residence time at high temperature in turbulent flames.

When measuring emission spectra in the optically accessible temperature-controlled furnace, it is not possible to limit the residence time to a few seconds. In order to obtain emission spectra without any thermal degradation occurring to the phosphor at temperatures above

770 K, a first approach was to quickly introduce the sample when the oven is already at high temperature. In this case, the temperature of the sample rises by 800 K over 150 s. However, the poor thermal conductivity of the powder stack due to the air present in the void between particles resulted in strong temperature gradients across the powder sample, leading to large measurement errors and a lack of repeatability. Instead, and in order to limit spectral shift and the reduction in phosphorescence intensity linked to thermal degradation, the oven was continuously flushed with a nitrogen flow of 15 SLPM. The sample was introduced when the furnace (Eurotherm 2416CG, Lenton Furnaces) was cold, and the temperature gradually increased to 1100 K. Spectra were recorded at intervals of 100 K. A thermocouple was embedded in the powder using high-temperature cement (Omegabond 400) so that its junction was located a few millimetres below the surface of the powder stack.

In order to assess possible thermal degradation, the sample was rapidly removed from the oven after taking the measurement at 1100 K. A very small blueshift (0.1 nm) with respect to the untreated sample was detected; however, this has almost no consequence on the evaluated ratio (<0.01 % deviation). For future comparison in terms of effective residence time, the treatment can be approximated by a linear increase in furnace temperature from 300 to 1100 K over 45 min before the sample was removed.

As in [1], the sample was excited at 355 nm with a fluence of 1 mJ/cm², and the emission spectra were measured using a 300 mm focal length spectrometer (Acton SP-2300i, Princeton Instruments) with a grating groove density of 300 g/mm, f/4 optics and an interline transfer CCD camera (Imager Intense, LaVision). The entrance slit width was 100 μm, providing a spectral resolution of 1 nm. The transmittance/quantum efficiency of the complete detection system was previously calibrated using the reference spectrum of a tungsten halogen lamp (LS-1, Ocean Optics).

3 Theoretical calculations

3.1 Calculation of the number of photons emitted by a single particle

By knowing the number of particle in a probe volume and the measured phosphorescence intensity, it is possible to estimate the number of photons emitted by a single particle. This value depends on the excitation process as well as on the fluid conditions (e.g. temperature, gas composition) but is independent of the detection system. Equation (1) is used to calculate the total emission intensity per particle. The values of the different parameters entering into this calculation are provided in Table 2. The camera responsivity (counts/photons) was measured experimentally using a NIST-calibrated integrating sphere (Labsphere LR-USS-8H) with a luminance detector. The filter transmission efficiency is computed by numerically integrating the product of the filter transmission function and the normalised phosphorescence spectrum, provided in [1]. The collection efficiency is estimated based on the diameter of the camera lens aperture and the object to lens distance.

$$N_{ph} = \frac{I_{pix} M_t^2}{\eta_F K_{cam} \eta_O N_p l_{pix}^2 t_L} \quad (1)$$

3.2 A statistical model for the measurement uncertainty

Once the influence of various parameters (temperature, laser fluence, seeding density) on the phosphorescence intensity is known, the performance of the technique can be predicted over a wide range of conditions, including for different detection systems and sets of interference filters, given that appropriate statistical models are employed.

A method for the prediction of the random temperature error is described below. If the intensity ratio is defined as the ratio of the intensities recorded in each channel, I_A and I_B :

Table 2 Nomenclature of Eq. 1 and values for the current set-up

Symbol	Description	Unit	Value
I_{pix}	Pixel intensity	Count	–
K_{cam}	Camera responsivity	Counts/photon	0.3
η_F	Filter transmission efficiency (photon transmitted per luminescence photon emitted at room temperature)		0.3
M_t	Magnification		0.3
η_O	Collection efficiency		1.7×10^{-3}
N_p	Particle number density	Particles/m ³	–
l_{pix}	Binned pixel size	μm	26
t_L	Sheet thickness	μm	600

Table 3 Parameters used in Eq. 7

Symbol	Description	Unit	Value
K	Conversion factor	Counts/electron	0.5
σ	Read-out noise	Counts	1.5
N_{av}	Size of the averaging kernel	Pixels	49

$$\varphi = \frac{I_B}{I_A} \quad (2)$$

then the uncertainty in the measured temperature can be estimated using a linearised error propagation theory [20] as in:

$$\sigma_T = \frac{dT}{d\varphi} \varphi \sqrt{\left(\frac{\sigma_{I_A}}{I_A}\right)^2 + \left(\frac{\sigma_{I_B}}{I_B}\right)^2} \quad (3)$$

where $\frac{1}{\varphi} \frac{d\varphi}{dT}$ is the temperature sensitivity of the filter combination, σ_{I_A} and σ_{I_B} are the uncertainty in the absolute intensity I_A and I_B , respectively. The term $\sqrt{\left(\frac{\sigma_{I_A}}{I_A}\right)^2 + \left(\frac{\sigma_{I_B}}{I_B}\right)^2}$ is the normalised ratio uncertainty $\frac{\sigma_\varphi}{\varphi}$, denoted η . For non-intensified CCD cameras, the uncertainty in the absolute intensity has contributions from the read-out noise and the photon (or shot) noise. The propagation of uncertainty for a sum of uncorrelated variables being the square root of the sum of the uncertainty of each variable, the uncertainty in the absolute intensity in each channel is:

$$\sigma_{I_i} = \sqrt{\sigma_{\text{readout}}^2 + \sigma_{\text{shot},i}^2} \quad \text{for } i = A, B \quad (4)$$

The contribution of the shot noise is dependent on the square root of the sampled quantity (photo-electrons) which after averaging and conversion results in:

$$\sigma_{\text{shot},i} = \sqrt{\frac{I_i}{K}} \times \frac{1}{\sqrt{N_{Av}}} \times K = \sqrt{\frac{KI_i}{N_{Av}}} \quad \text{for } i = A, B \quad (5)$$

where K is the conversion factor of the analog–digital converter (counts/e-) and N_{av} is the number of pixels in the averaging kernel. The read-out noise is independent of the photon flux. After spatial filtering, its contribution is:

$$\sigma_{\text{readout}} = \frac{\delta}{\sqrt{N_{Av}}} \quad (6)$$

where δ is the single pixel read-out noise of the camera (in counts). Combining Eqs. 3–6, the normalised ratio uncertainty can be written as:

$$\eta = \sqrt{\frac{1}{N_{Av}} \left(\frac{\delta^2 + KI_A}{I_A^2} + \frac{\delta^2 + K\varphi I_A}{(\varphi I_A)^2} \right)} \quad (7)$$

The camera read-out noise is measured as the spatially averaged pixel-to-pixel standard deviation of the recorded intensity, while the camera lens is capped. The conversion factor is determined by dividing the measured camera responsivity (see Sect. 3.1) by the quantum efficiency provided by the camera manufacturer. The numerical values for these terms can be found in Table 3.

As shown in Eqs. 3 and 7, the dependence of the random measurement uncertainty on the temperature can be attributed to three terms I_A , φ and $\frac{dT}{d\varphi}$, which are strongly temperature-dependent.

The next step is to determine the pixel intensity I_A for the given conditions. The influence of various parameters on the recorded intensity is summarised in Eq. 8.

$$I_A = I_{A,\text{ref}} \times \frac{N_p}{N_{p,\text{ref}}} \times \frac{\int_0^\infty E(\lambda, T) \tau_A(\lambda) d\lambda}{\int_0^\infty E(\lambda, T) d\lambda} \times \frac{\int_0^\infty E(\lambda, T_{\text{ref}}) d\lambda}{\int_0^\infty E(\lambda, T_{\text{ref}}) \tau_{A,\text{ref}}(\lambda) d\lambda} \times \frac{Q(T)}{Q(T_{\text{ref}})} \times \frac{S(F)}{S(F_{\text{ref}})} \quad (8)$$

N_p is the seeding density, $E(\lambda, T)$ is the spectral radiance at the input of the spectrometer in Sect. 2.6, τ_A is the transmission function of the filter and beam splitter in channel A, Q is a function accounting for the drop in the total emission intensity per particle with temperature, and S a function accounting for the dependence of the total emission intensity with fluence F . Ref describes a reference condition at which the absolute intensity $I_{A,\text{ref}}$ is measured. The third term is the collection efficiency of the chosen filter combination at a given temperature, while the fourth term is the inverse of the collection efficiency of the reference filter combination at the reference temperature.

The temperature sensitivity is:

$$\frac{1}{\varphi} \frac{d\varphi}{dT} = \frac{d(\ln(\varphi))}{dT} \quad (9)$$

The intensity ratio φ is computed from the transmission functions of the interference filters and the emission spectra obtained at various temperatures (Sect. 4.2.1) as in:

$$\varphi(T) = \frac{\int_0^\infty E(\lambda, T) \tau_B(\lambda) d\lambda}{\int_0^\infty E(\lambda, T) \tau_A(\lambda) d\lambda} \quad (10)$$

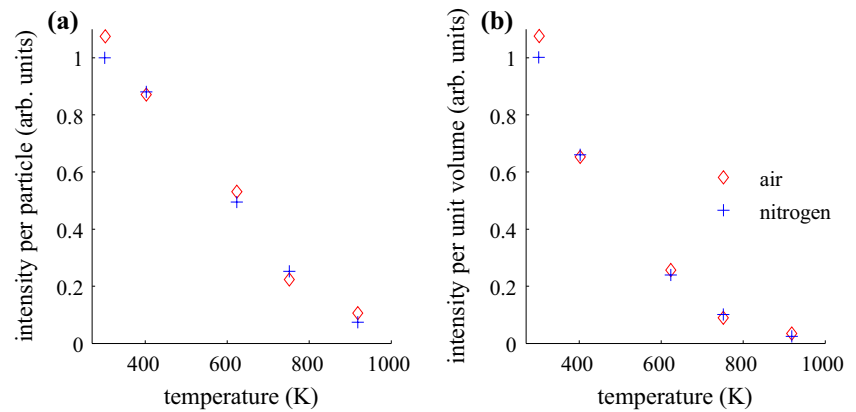
4 Results

4.1 Luminescence intensity

4.1.1 Absolute luminescence intensity

By simultaneously measuring the luminescence intensity and the seeding density using the particle-counting system, the total emission intensity per particle can be estimated

Fig. 3 Normalised intensity per particle (a) and per unit volume (b) as a function of temperature obtained in heated streams of air (diamonds) or pure nitrogen (crosses)



following the approach described in Sect. 3.1. Results presented in our recent study [14] indicated that at a fluence of 23 mJ/cm^2 and at room temperature, a seeding density of 10^{11} particles per m^3 resulted in a pixel intensity of 200 counts in the 464–40 channel. From this result, it can be estimated that a single BAM:Eu²⁺ particle emits on average 3×10^6 luminescence photons following a single laser pulse.

This result is of fundamental interest to quantify the interaction between a pulsed laser beam and a single particle. In addition, being independent of the detection system, this result can be used to estimate signal levels for other measurement configurations.

4.1.2 Dependence of luminescence intensity on excitation fluence

The effect of the laser fluence on the luminescence intensity was first reported in [1] and then quantified using the particle-counting system in [14]. An obvious nonlinear dependence was observed at fluences above 5 mJ/cm^2 , and it was shown that at 400 mJ/cm^2 , the luminescence intensity is more than 10 times less as expected from a linear behaviour at low fluences, providing evidence of a saturation phenomena. This behaviour is explored in detail in Sect. 4.4.

4.1.3 Dependence of luminescence intensity on temperature and oxygen concentration

Simultaneous measurements of luminescence intensity and seeding density were performed in the heated jet configuration described above in order to determine the evolution of the intensity per particle with temperature. As shown in Fig. 3a, at 920 K, the particle luminescence intensity is 9 % of the room-temperature intensity. If the drop in particle number density due to the gas expansion is also accounted for, then the drop in phosphorescence intensity per unit volume can be determined, as shown in Fig. 3b. At 920 K,

the intensity per unit volume is 3 % of the room-temperature value. Note that this range of intensities is within the dynamic range of these cameras (12 bits).

Some phosphors, e.g. Y₂O₃:Eu³⁺, were reported to be sensitive to the gas composition [22], although no physical mechanism for this was proposed. Here, the sensitivity of the phosphorescence intensity to the concentration of oxygen was investigated by measuring in air and in pure nitrogen. The results are also shown in Fig. 3. The presence of oxygen up to atmospheric concentrations does not have a measurable effect on the phosphorescence intensity. The deviations between the two cases are within the experimental uncertainty. This is a significant advantage of this tracer over most LIF tracers, which are strongly quenched by oxygen, see e.g. [17].

4.2 Measurement precision

4.2.1 Emission spectrum

Phosphorescence emission spectra plotted at 200 K intervals are shown in Fig. 4. These results demonstrate that using appropriate filters, the ratio response is a monotonic function of temperature up to 1100 K.

4.2.2 Achievable temperature precision

These spectral measurements can be combined with the estimation of the absolute luminescence intensity at various temperatures to find an optimum filter set and determine the level of precision which can be achieved over this range. However, these estimations must rely on an accurate model for the measurement uncertainty.

In a recent study [14], we measured simultaneously seeding density and measurement precision in order to quantify the performance offered by a given phosphor and detection system combination. In Fig. 5, these measurements are plotted in terms of pixel intensity and normalised ratio precision and compared to the statistical model

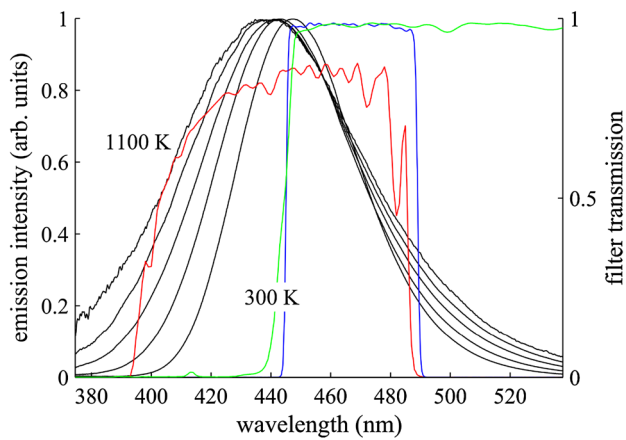


Fig. 4 Emission spectrum of BAM:Eu²⁺ recorded at 200 K interval in Nitrogen (1 nm spectral resolution). The transmission profiles of the filters (as provided by the manufacturer) used in this study are shown in colour: *red*: 440-90 nm (notation CWL-FWHM) *blue* 464-40 nm (notation CWL-FWHM). The transmission profile of the dichroic beam splitter t445lp is shown in *green*

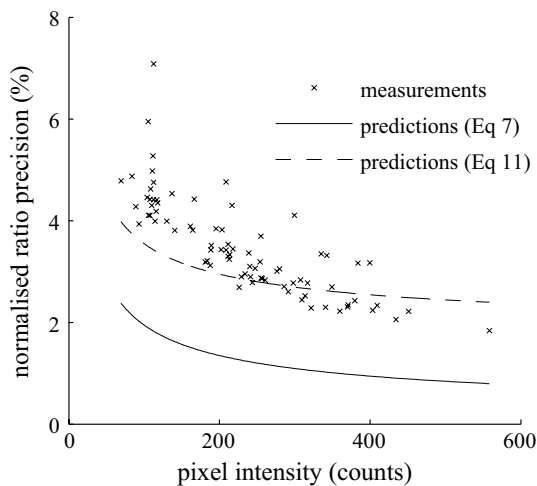


Fig. 5 Normalised ratio precision obtained for varying pixel intensities, for an intensity ratio of 0.4. The theoretical ratio precision calculated from Eq. 7 and from Eq. 11 are also plotted

Table 4 Predictions of the temperature sensitivity, pixel intensity and temperature precision for different experimental conditions, and virtual filter sets representative of commercially available filters. All fil-

Temp (K)	Seeding density (/m ³)	Filter 1 CWL-BW	Filter 2 CWL-BW	Sensitivity (%/K)	IA (cts)	IB (cts)	Precision (K)
293	1 × 10 ¹¹	466-40	440-90	0.24	186	136	11 K (3.7 %)
293	1 × 10 ¹¹	460-10	420-30	0.35	57	75	10 K (3.3 %)
293	1 × 10 ¹¹	466-40	436-140 ^a	0.24	186	138	11 K (3.7 %)
920	8 × 10 ¹¹	466-40	440-90	0.05	128	173	55 K (6.1 %)
920	8 × 10 ¹¹	460-10	420-30	0.06	38	110	60 K (10.8 %)
920	8 × 10 ¹¹	466-40	436-140 ^a	0.07	128	173	40 K (4.6 %)

^a This filter represents a 355-nm notch filter, e.g. Edmund Optics #67106

described in Sect. 3.2 which is based on signal statistics. This figure shows that the random uncertainty originating from the propagation of detector noise (Eq. 7) accounts for a significant part (>50 %) of the measured precision. The remainder indicates the presence of other contributions which can originate, for example, from a residual displacement between the images before division, or from particle-to-particle variation in the luminescence properties. To account for these contributions, a intensity-independent term ε was added to the random uncertainty calculated from Eq. 7:

$$\eta_{tot} = \eta + \varepsilon \quad (11)$$

The results of Eq. 11 for a fixed error contribution of 1.6 % are shown on Fig. 5. Measurements and predictions now agree reasonably well. The remaining deviations can be explained by the fact that residual errors are in this case also intensity dependent. It is indeed evident that the error originating from residual image displacement and particle-to-particle variations should decrease with the number of particles in the image, and therefore with the intensity in the present case. With increasing number of particles in the image, the illumination becomes less structured, so the effects of misalignment on the result of the image division are lower. In addition, if there are particle-to-particle variations in the luminescence emission, the effect will also decrease with averaging. Further efforts will be placed in the investigation of these sources of errors to offer a refinement of the model using a seeding-density-dependent term.

The results of the quantitative investigation performed in the sections above can now be combined to establish the performance and limits of the technique. Results are shown on Table 4, noting that the temperature precision was calculated using:

$$\sigma_T = \frac{dT}{d\varphi} \varphi(\eta + \varepsilon) \quad (12)$$

In Table 4, the performance of three filter sets is provided at 300 and 900 K. In general, at room temperature,

ter sets have a top hat transmission profile, with a peak transmission of 90 % and are combined with a dichroic beam splitter (t445lp). The fluence is 20 mJ/cm²

a high level of precision of about 4–5 % can be obtained with a seeding density as low as 10^{11} particles per m^3 , as previously reported in [14]. This seeding density was then judged moderate, since it is similar to the minimum seeding density required for PIV measurement at the same spatial resolution 600 microns, and because it has negligible effects on the gas thermal properties. These results are the consequence of a high luminescence output combined with an efficient detection system. Phosphors with unfavourable luminescence properties will require excessively high seeding density to reach a sufficient signal level. These may result in particle-induced changes of the gas thermal properties and potentially the quenching of chemical reactions. Excessive seeding densities can also decrease the resolution of the technique due to multiple scattering of both the excitation light and the emitted luminescence by other particles throughout the entire measurement plane. For these reasons, every phosphor should be characterised in this manner, to determine its suitability for gas-phase measurements.

The comparison between the three filter sets in Table 4 illustrates the compromise between sensitivity and signal level. The narrow filter combination (420–10 and 460–10) offers a high sensitivity at room temperature (0.35 %/K) compared to the wider filter set (440–90 and 464–40) used in this study. However, the integrated signal is far lower, which overall results in a similar temperature precision (11 K versus 10 K at 300 K).

All three filter sets suffer from a loss of sensitivity as the temperature increases, which is easily understood by looking at the spectral data (see Fig. 4). The broadening of the emission spectrum towards the UV region is relatively linear with temperature, so the relative area increase in the short-pass channel drops as the total area in that channel increases.

At higher temperature, the filter set including a 355 nm notch filter, represented here by the virtual 436–140 nm which fully integrates the blue broadening of the emission spectrum, offers a significant improvement over the two other filter sets. Using this combination, a precision of 40 K can be achieved at 920 K at a seeding density of 8×10^{11} particles/ m^3 . At this level of seeding and for this temperature, the heat capacity of the gas is increased by 2.2 %. Our conclusion is that for higher temperatures, another phosphor material is required, which possesses either a delayed onset of thermal quenching, i.e. which is brighter at higher temperature, or a higher temperature sensitivity.

4.3 Measurement accuracy

In this section, the influences of seeding density, oxygen partial pressure and excitation fluence on the measured temperature

are investigated in order to determine potential sources of uncertainty linked to the photo-physics of the particles.

4.3.1 Effect of the seeding density on the intensity ratio

If the excitation and emission spectra of the thermographic phosphor tracer particles overlap, re-absorption of phosphorescence light can occur, and the detected phosphorescence spectrum may be dependent on the number density and the optical path through the seeded flow of interest since part of the spectrum will be more absorbed. In addition, the Mie scattering cross section is, albeit weakly, wavelength-dependent, and for particles with a broad emission spectrum, elastic scattering can potentially alter the spectrum of the collected light. For BAM:Eu²⁺, there is only a small overlap between excitation and emission spectrum in the region from 400 to 425 nm (see Figs. 4, 9). For this study the effect of the seeding density on the measured temperature was quantified using the two-camera phosphorescence detection and particle-counting systems for a seeded flow above a 40 mm diameter nozzle, with the laser sheet crossing the jet centreline. Results are presented in Fig. 6. A weak trend can be observed, but given the uncertainty resulting from the camera linearity calibration (2 % in camera gain or 15 K in temperature after division and conversion), we cannot conclude on an actual effect of the seeding density, over the indicated range of seeding density and for a 20 mm optical path through the seeded jet.

4.3.2 Effect of the oxygen partial pressure on the intensity ratio

The sensitivity of the intensity ratio to the oxygen concentration was investigated over the temperature range

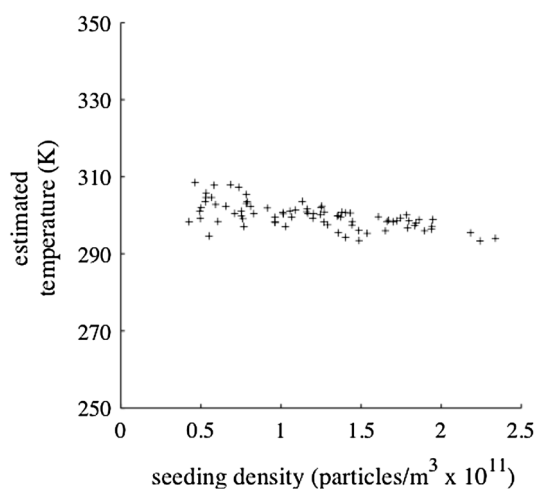


Fig. 6 Measured temperature as a function of the seeding density. The exit jet temperature is 293 K

300–950 K; see Fig. 7. As with the absolute intensity, the intensity ratio response is also unaffected by oxygen concentrations over the tested range (O₂ partial pressure from 0 to 200 mbar). Therefore, this phosphor can be used for thermometry in flows with oxygen concentration variations. Another study performed in an oxygen-free environment has also shown that the luminescence of BAM:Eu²⁺ is insensitive to pressure up to 1000 bar [23].

With the filter combination used in this study, the sensitivity of the phosphor to temperature drops significantly above 800 K. As discussed in Sect. 4.2.2, this is partly due to the filter combination, which does not integrate the blue broadening of the emission spectrum in the region below 395 nm. A filter combination involving a 355-nm notch filter was proposed in Sect. 4.2.2 to improve the sensitivity at higher temperatures.

4.3.3 Effect of the excitation fluence on the intensity ratio

A potential dependence of the measured temperature on the excitation fluence was explored by measuring the intensity ratio with increasing excitation fluence and converting it to temperature using calibration data obtained at 20 mJ/cm². Figure 8 shows an increase of 50 K in the measured temperature when increasing the excitation fluence from 1 to 400 mJ/cm². Beyond 200 mJ/cm², the influence becomes very weak. These results disagree with previous studies including ours [1, 24]. However, it is likely that this weak trend was not observed in the aforementioned studies due to low signal levels.

It must be noted that, for practical applications, if the calibration and the actual measurements are performed at similar fluence, this dependence on the laser fluence will have a negligible effect on the measurement accuracy.

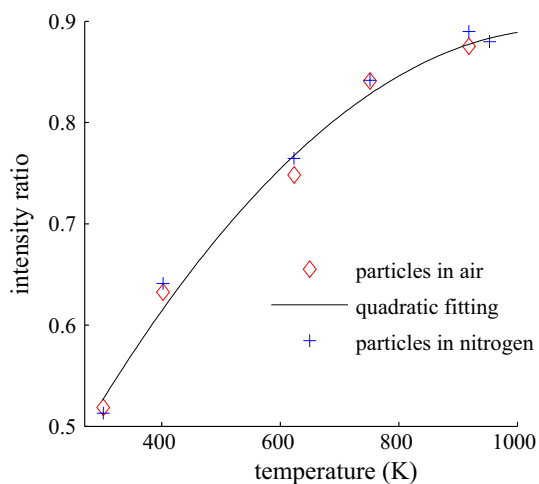


Fig. 7 Intensity ratio as a function of temperature measured in a stream of air and in a stream of nitrogen

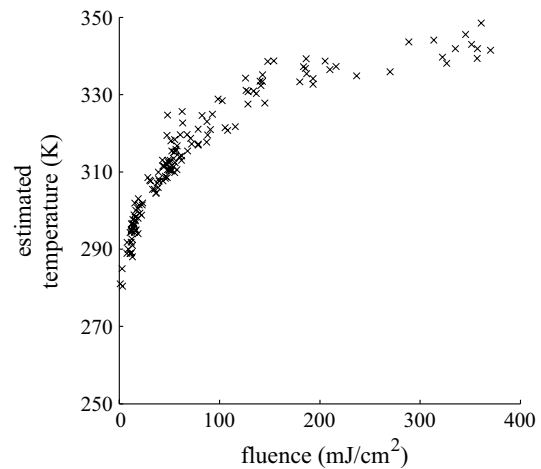


Fig. 8 Measured temperature as a function of the excitation fluence using calibration data obtained at a 20 mJ/cm². The jet exit temperature is 293 K

For example, a 10 % variation in the laser fluence (e.g. due to pulse–pulse fluctuations, or spatial variations of the fluence within the laser sheet profile) at a mean fluence of 50 mJ/cm² leads to a temperature variation of <2 K.

From the results of the Sects. 4.2 and 4.3, the total uncertainty can be estimated in a given measurement situation. It is the sum of the random uncertainty or precision, as calculated using the model described in Sect. 3.2, and of systematic errors, which can originate for instance from errors in camera linearity, or from laser fluence effects.

4.4 Investigating the saturation of the phosphorescence emission

At elevated temperatures, signal levels are expected to be the limiting factor for the measurement precision due to the quenching of the luminescence emission and the drop in gas density (see Sect. 4.1.3). Because the luminescence saturates (nonlinear dependence of the phosphorescence intensity on the excitation fluence), the signal level cannot be increased simply by increasing the pulse energy of the laser. Using flashlamp-pumped Nd:YAG lasers, high fluences (~400 mJ/cm²) can be achieved, but operating at these levels does not provide much gain in signal. One can claim that if the causes of saturation were better understood, changes in the dopant concentration or excitation schemes could be proposed which may extend the linear regime to higher fluences and in this sense, and could offer large gain in signal at these higher fluence levels. The next section discusses possible explanations for saturation and presents the results of experiments performed

using different excitations schemes in an attempt to achieve higher signal levels.

Saturation phenomena were observed for several plasma display panel phosphors including BAM:Eu²⁺ and Y₂O₃:Eu³⁺ under vacuum UV excitation [25]. Three plausible mechanisms for intrinsic saturation phenomena in inorganic phosphors are proposed in the literature: activator ground-state depletion [26–28], excited-state interaction [28, 29] and quenching due to laser-induced temperature rise [28]. Each is explored below, in the context of this particular phosphor and in view of the various results presented in this paper.

The temperature rise mechanism is explored first. The increase in laser fluence leads to an increase in the particle temperature since part of the photon energy is deposited in the particle due to the difference in excitation and emission photon energy. Also, some of the excitation photons are absorbed and deposit their energy in the particle via non-radiative relaxation (QE < 1). As the particle temperature is increased, the quantum efficiency of the phosphor drops, and so the rate of increase in the luminescence intensity with the laser fluence decreases. From the increase in measured temperature with fluence (Fig. 8), and the drop of luminescence intensity with temperature (Fig. 3), the expected drop in quantum efficiency due to the particle being heated up by the laser should be no more than 20 %, which does not support this scenario. Also, the rate of increase in the measured temperature should increase with excitation fluence, as the quantum efficiency drops, resulting in additional heat dissipation. The results of Fig. 8 show the exact opposite. Beyond 200 mJ/cm², the fluence has little effect on the measured temperature.

A cross relaxation or excited-state interaction phenomena was found to play a major role in the saturation of Y₂O₂S:Eu³⁺ [28] and Tb³⁺-doped phosphors [29]. As more atoms are promoted to the excited state, the mean distance between excited luminescent centres increases, and energy transfer between excited Eu²⁺ ions may occur. One ion gives away its excess energy to a neighbouring excited ion, returning to the ground state without emitting a photon and promoting the other ion to a higher excited state. This process is then followed by a fast non-radiative transition to its former lower excited state from which it may relax back to the ground state via either a radiative or non-radiative transition. This process would result, at best, in the emission of a single photon for two absorbed photons. In this situation, the quantum efficiency of the phosphor would also decline with laser fluence due to an increase in non-radiative relaxation. The fact that the measured temperature stops increasing with laser fluence also contradicts this explanation.

The third possibility is that as the laser fluence increases, the number of photons absorbed by a BAM:Eu²⁺ particle increases, which depopulates the absorbing state of the

Eu²⁺ atoms. This results in a decrease in the absorption probability. In this respect, one could interpret the trend of Fig. 8 as the result of a drop in absorption cross section with laser fluence. In other words, no more luminescent centres can be excited, and the material becomes transparent for the excitation wavelength, allowing no further heat dissipation.

In order to explore this explanation further, the number of photons emitted by a single particle after a single excitation pulse can be compared to the number of excitable ions in a particle. Because the excitation pulse duration (7 ns) is much shorter than the luminescence lifetime (~1 μs), it is assumed for simplicity that each atom can be excited only once during the excitation pulse. An energy-dispersive X-ray analysis indicated that the europium content is between 9 and 11 %. Considering a 2 μm diameter spherical particle with a europium content of 10 % (Ba_{1-x}Eu_xMgAl₁₀O₁₇, x = 0.1) and that all europium atoms are excited and then decay via photon emission (quantum efficiency >90 % [16]), 10⁹ photons should be emitted at room temperature. In Sect. 4.1, we measured that a particle emits on average 3 × 10⁶ photons per laser pulse in the saturated regime (23 mJ/cm²). This difference of around a factor of 300 is too large to confirm the hypothesis of a ground-state depopulation and too small to refute it. Indeed, it may not be possible to excite all the europium atoms using the current excitation wavelength of 355 nm. In addition, this calculation is associated with large uncertainties since the particles are non-spherical (see Fig. 1) with dimensions that are widely distributed so the average volume of the particles under investigation could be significantly lower than that of a 2 μm diameter sphere.

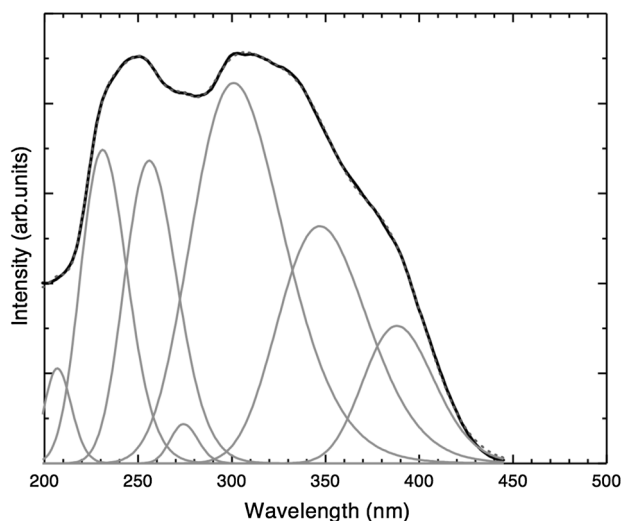


Fig. 9 Typical excitation spectrum of BAM:Eu²⁺ resolved into seven Gaussian bands. Emission collected at 460 nm. Reproduced with permission from [30]

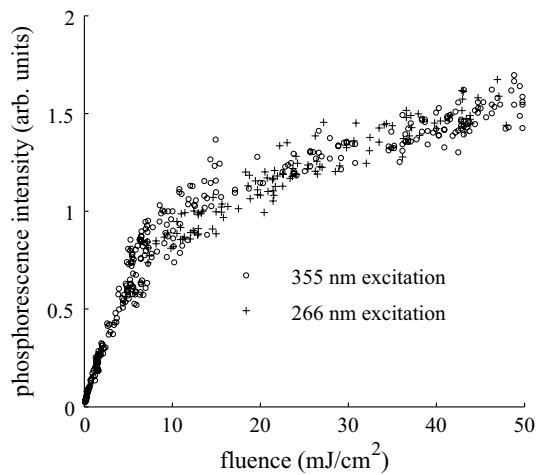


Fig. 10 Phosphorescence emission intensity on a per-particle basis under increasing excitation fluence for both 355 and 266 nm excitation

Many studies suggest that europium ions reside in different sites in the BAM lattice [21, 23, 30–32]. The crystal field acting on the Eu²⁺ atoms differs between sites so that the asymmetrical emission spectrum is interpreted as a convolution of the Gaussian-shaped emission spectra of these different sites [21]. It is also proposed that the very broad and irregular excitation spectrum above 200 nm shown in Fig. 9 is composed of the absorption bands of the individual sites [30]. The excitation below 200 nm is attributed to host lattice absorption. Based on this reasoning, it may be possible to access different sites using different excitation schemes. These sites might have different populations, and the saturation threshold could potentially be increased. The aforementioned studies [21, 23, 30–32] agree on the existence of at least three sites named Beever–Ross (BR), anti-Beever–Ross (aBR) and mid-Oxygen (mO). However, the position, strength, and width of the absorption band of each site are still not completely clear. We investigate this hypothesis by exciting the phosphor particles at 266 and 355 nm. According to Refs. [19, 30], the 355 nm light should be absorbed in the mO site, while the 266 nm laser should excite the aBR site.

The luminescence emission intensity under each excitation scheme was compared at various fluences, and the results are presented in Fig. 10. The results show that the luminescence intensity is very similar for the two excitation schemes, with similar nonlinear dependence on the excitation fluence above 10 mJ/cm². This result suggests that either the same sites are excited at 266 and 355 nm, or that two different sites with a similar population were involved. Combining the difference in photon energy between the two wavelengths and the improved excitation characteristics at 266 nm, a similar number of photons should be

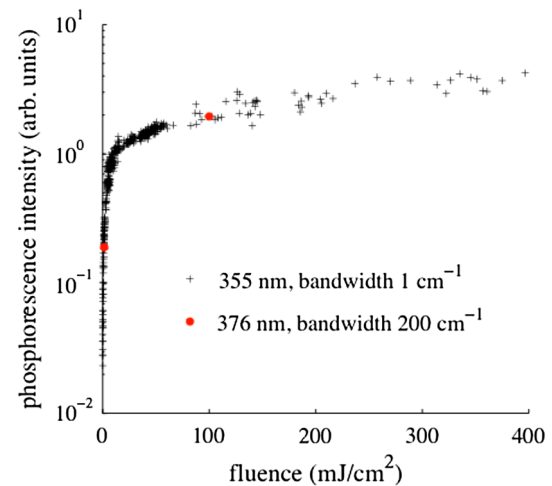


Fig. 11 Normalised phosphorescence intensity per particle under conventional frequency-tripled Nd:YAG laser (1 cm⁻¹ bandwidth at 355 nm) and under broadband dye laser excitation (200 cm⁻¹ bandwidth at 376 nm)

absorbed at a given fluence for the two schemes. Note that it is not possible to use the emission spectrum to distinguish between absorbing sites as it is insensitive to the excitation wavelength. This is likely caused by energy transfer occurring between sites over the relatively long time spent in the excited state (around 1 μs lifetime).

In inorganic solids, due to the various positions of the luminescent centres within the crystal, the local crystal field is different for each emitter, resulting in slightly differing positions of the energy levels due to the Stark effect. This is referred to as inhomogeneous spectral broadening. If the natural linewidth of the absorption transition is narrow, then inhomogeneous broadening can be responsible for the broad excitation spectrum. The Nd:YAG laser used here has a spectral bandwidth of <1 cm⁻¹. This may imply that only europium ions influenced by a specific crystal field will absorb the laser energy, and these ions may represent only a portion of the europium ions present in the particles. To assess this assumption, the broadband dye laser source was used with a much larger spectral bandwidth of 200 cm⁻¹. The luminescence emission intensity under both excitation schemes were compared at two different excitation fluences.

Figure 11 shows that this light source does not increase the luminescence intensity in the saturated regime. The 4f⁷ → 4f⁶5d excitation transition of the divalent europium ion is parity allowed but partially spin forbidden. This may result in a relatively large natural linewidth of the transition, so that no additional atoms are excited by the larger bandwidth of the 376 nm laser.

Neither of the two excitation schemes investigated here offer any improvement with respect to the saturation

behaviour of the luminescence emission. Without performing a full excitation scan at high fluences, using, e.g. a dye laser or an optical parametric oscillator (OPO), one cannot definitely rule out the existence of a more populous site being accessible via another excitation wavelength.

It is expected that longer pulse durations would offer improvements in term of luminescence intensity at high fluence level. Relatively simple pulse stretchers are more commonly used in flow diagnostics [33, 34], to increase the pulse duration from about 5 ns to 10's or 100's of ns. Their impact on the luminescence intensity of BAM:Eu²⁺ should be investigated, particularly at higher temperature where the luminescence lifetime is shorter, and the signal limited.

5 Conclusions

In this paper, the luminescence properties of BAM:Eu²⁺ tracer particles were characterised in the gas phase, in the context of thermographic particle image velocimetry, through a number of experiments and theoretical considerations. The methodology for the characterisation of thermographic phosphor tracer particles described in [14] was applied to 2 μm BAM:Eu²⁺ particles. This method consists of experiments in the gas phase, with the simultaneous measurement of the seeding density.

First, the emission intensity (number of photon emitted by a single particle) was measured, and its dependence on parameters such as the gas composition and the temperature were described. A single BAM:Eu²⁺ particle emits on average 3×10^6 photons per excitation pulse at room temperature for an excitation fluence of 23 mJ/cm². This results in high signal levels at moderate seeding densities.

The luminescence intensity is independent of the oxygen partial pressure over the range investigated (0–200 mbar). This is in contrast with most LIF tracers, which are strongly quenched by oxygen. The luminescence intensity per particle decreases with temperature, also called thermal quenching, which currently limits the upper temperature range of this phosphor. At 920 K, the intensity is 9 % of the room-temperature value. The luminescence intensity is shown to saturate, i.e. the emitted intensity has a sub-linear dependence on excitation fluence over 10 mJ/cm².

Spectrally resolved measurements performed on the phosphor in powder form in an optically accessible oven flushed with a flow of nitrogen to avoid thermal degradation show that the emission spectrum continuously shifts and broadens towards the UV from 300 to 1100 K.

The knowledge of the emission intensity per particle and the spectral response to temperature allows the accurate theoretical prediction of the achievable temperature precision under different conditions and for different detection systems. With the detection system used in this article and

a suggested filter combination, a 45-K precision is expected at 920 K for a seeding density of 8×10^{11} particles per m³. For higher temperatures, another phosphor material with delayed onset of thermal quenching or improved temperature sensitivity should be investigated.

For a complete uncertainty analysis, dependency of the measured temperature on the seeding density, the oxygen partial pressure and the excitation fluence are explored. While the seeding density and the oxygen partial pressure have negligible effect, a dependence of the measured temperature on the excitation fluence was observed, but the effect on the measurement accuracy is negligible provided that care is taken to limit the range of fluences used in a series of measurements.

Finally, in an attempt to increase signal levels at higher temperature, the photo-physics behind the observed saturation behaviour of the luminescence emission are investigated. Mechanisms (ground-state depopulation, laser-induced heating, and internal conversion) are suggested and discussed. A depopulation of the ground state appeared likely. Based on the hypothesis, that not all europium atoms are probed under the current excitation scheme, two additional excitation schemes were used (narrowband 266 nm, and broadband 376 nm). Unfortunately, no gain in luminescence intensity was observed with these alternative schemes. Additional insight is required, using for example, other excitation wavelengths, or longer pulse durations.

These studies clearly show that BAM:Eu²⁺ is a robust tracing material for thermographic particle image velocimetry, capable of providing accurate temperature measurements up to 900 K.

The results presented in this article also serve as a guide for the future users of this tracer material for precise temperature and velocity imaging in turbulent flows. It allows the prediction of signal levels, measurement precision and accuracy for a wide range of conditions.

A very attractive aspect of the use of thermographic phosphor tracer particle for gas-phase diagnostics is that there is an almost infinite number of phosphors, involving a wide range of luminescence mechanisms, and capable of covering various temperature range and degrees of sensitivity. A specific phosphor can then be used for a specific application. In this respect, the same tests are being performed on new phosphor materials which promise much improved temperature sensitivity, e.g. ZnO [13].

Acknowledgments The authors gratefully acknowledge the financial support of the UK Engineering and Physical Science Research Council (EPSRC) for parts of this work.

Open Access This article is distributed under the terms of the Creative Commons Attribution 4.0 International License

(<http://creativecommons.org/licenses/by/4.0/>), which permits unrestricted use, distribution, and reproduction in any medium, provided you give appropriate credit to the original author(s) and the source, provide a link to the Creative Commons license, and indicate if changes were made.

References

1. B. Fond, C. Abram, A.L. Heyes, A.M. Kempf, F. Beyrau, Simultaneous temperature, mixture fraction and velocity imaging in turbulent flows using thermographic phosphor tracer particles. *Opt. Express* **20**, 22118–22133 (2012)
2. A. Omrane, P. Petersson, M. Alden, M.A. Linne, Simultaneous 2D flow velocity and gas temperature measurements using thermographic phosphors. *Appl. Phys. B* **92**, 99–102 (2008)
3. N.J. Neal, J. Jordan, D. Rothamer, Simultaneous measurements of in-cylinder temperature and velocity distribution in a small-bore diesel engine using thermographic phosphors. *SAE Int. J. Engines* **6**, 300–318 (2013)
4. S. Someya, Y. Okura, M. Uchida, Y. Sato, K. Okamoto, Combined velocity and temperature imaging of gas flow in an engine cylinder. *Opt. Lett.* **37**, 4964–4966 (2012)
5. C. Abram, B. Fond, A.L. Heyes, F. Beyrau, High-speed planar thermometry and velocimetry using thermographic phosphor particles. *Appl. Phys. B* **111**, 155–160 (2013)
6. A.O. Ojo, B. Fond, B.V. Wachem, A.L. Heyes, F. Beyrau, Thermographic laser doppler velocimetry. *Opt. Lett.* **40**, 4759–4762 (2015)
7. R. Hasegawa, I. Sakata, H. Yanagihara, G. Särner, M. Richter, M. Aldén, B. Johansson, Two-dimensional temperature measurements in engine combustion using phosphor thermometry. *SAE Paper 2007-01-1883*, 1797–1803 (2007)
8. R. Hasegawa, I. Sakata, H. Yanagihara, B. Johansson, A. Omrane, M. Alden, Two-dimensional gas-phase temperature measurements using phosphor thermometry. *Appl. Phys. B* **88**, 291–296 (2007)
9. D.A. Rothamer, J. Jordan, Planar imaging thermometry in gaseous flows using upconversion excitation of thermographic phosphors. *Appl. Phys. B* **106**, 435–444 (2012)
10. J. Jordan, D.A. Rothamer, Pr:YAG temperature imaging in gas-phase flows. *Appl. Phys. B* **110**, 285–291 (2013)
11. J.P.J. van Lipzig, M. Yu, N.J. Dam, C.C.M. Luijten, L.P.H. de Goey, Gas-phase thermometry in a high-pressure cell using BaMgAl₁₀O₁₇:Eu as a thermographic phosphor. *Appl. Phys. B* **111**, 469–481 (2013)
12. M. Lawrence, H. Zhao, L. Ganippa, Gas phase thermometry of hot turbulent jets using laser induced phosphorescence. *Opt. Express* **21**, 12260–12281 (2013)
13. C. Abram, B. Fond, F. Beyrau, High-precision flow temperature imaging using ZnO thermographic phosphor tracer particles. *Opt. Express* **23**, 19453–19468 (2015)
14. B. Fond, C. Abram, F. Beyrau, On the characterisation of tracer particles for thermographic particle image velocimetry. *Appl. Phys. B* **118**, 393–399 (2015)
15. I. Kamma, P. Kommidi, B.R. Reddy, High temperature measurement using luminescence of Pr³⁺ doped YAG and Ho³⁺ doped CaF₂. *Phys. Status Solidi C* **6**, S187–S190 (2009)
16. S. Shionoya, W.M. Yen, H. Yamamoto, *Phosphor Handbook* (CRC Press, Boca Raton, 2006)
17. C. Schulz, V. Sick, Tracer-LIF diagnostics: quantitative measurement of fuel concentration, temperature and fuel/air ratio in practical combustion systems. *Prog. Energy Combust.* **31**, 75–121 (2005)
18. S. Pfadler, F. Dinkelacker, F. Beyrau, A. Leipertz, High resolution dual-plane stereo-PIV for validation of subgrid scale models in large-eddy simulations of turbulent premixed flames. *Combust. Flame* **156**, 1552–1564 (2009)
19. Y.H. Wang, Z.H. Zhang, Luminescence thermal degradation mechanism in BaMgAl₁₀O₁₇:Eu²⁺ phosphor. *Electrochem Solid State* **8**, H97–H99 (2005)
20. G. Bizarri, B. Moine, On BaMgAl₁₀O₁₇:Eu²⁺ phosphor degradation mechanism: thermal treatment effects. *J. Lumin.* **113**, 199–213 (2005)
21. Y. Kim, S. Kang, Investigation of the degradation mechanisms in BaMgAl₁₀O₁₇:Eu²⁺ phosphor: on the influence of thermal process on operational durability. *Appl. Phys. B* **98**, 429–434 (2010)
22. J. Brubach, A. Dreizler, J. Janicka, Gas compositional and pressure effects on thermographic phosphor thermometry. *Meas. Sci. Technol.* **18**, 764–770 (2007)
23. R. Turos-Matysiak, M. Grinberg, J.W. Wang, W.M. Yen, R.S. Meltzer, Luminescence of BAM under high pressure: the Eu²⁺ sites. *J. Lumin.* **122**, 107–109 (2007)
24. J. Linden, N. Takada, B. Johansson, M. Richter, M. Alden, Investigation of potential laser-induced heating effects when using thermographic phosphors for gas-phase thermometry. *Appl. Phys. B* **96**, 237–240 (2009)
25. C. Okazaki, M. Shiiki, T. Suzuki, K. Suzuki, Luminance saturation properties of PDP phosphors. *J. Lumin.* **87–9**, 1280–1282 (2000)
26. S. Mikoshiba, S. Shirai, S. Shinada, M. Fukushima, Saturation of Zn₂SiO₄-Mn luminescence under intense VUV excitation. *J. Appl. Phys.* **50**, 1088–1090 (1979)
27. D.B.M. Klaassen, T.G.M. Vanrijn, A.T. Vink, A universal description of the luminescence Saturation behavior per phosphor. *J. Electrochem. Soc.* **136**, 2732–2736 (1989)
28. S. Imanaga, S. Yokono, T. Hoshina, Luminescence saturation effects in Y₂O₂S-Eu phosphor. *Jpn. J. Appl. Phys.* **19**, 41–49 (1980)
29. K.J.B.M. Nieuwesteeg, R. Raue, On the saturation of Tb phosphors under cathode-ray excitation. 2. Upconversion processes in the excited-activator bath. *J. Appl. Phys.* **68**, 6058–6065 (1990)
30. K.C. Mishra, M. Raukas, A. Ellens, K.H. Johnson, A scattered wave model of electronic structure of Eu²⁺ in BaMgAl₁₀O₁₇ and associated excitation processes. *J. Lumin.* **96**, 95–105 (2002)
31. A. Ellens, F. Zwaschka, F. Kummer, A. Meijerink, M. Raukas, K. Mishra, Sm²⁺ in BAM: fluorescent probe for the number of luminescing sites of Eu²⁺ in BAM. *J. Lumin.* **93**, 147–153 (2001)
32. P. Boolchand, K.C. Mishra, M. Raukas, A. Ellens, P.C. Schmidt, Occupancy and site distribution of europium in barium magnesium aluminate by Eu-151 Mossbauer spectroscopy. *Phys Rev B* **66**, 134429 (2002)
33. J. Kojima, Q.V. Nguyen, Laser pulse-stretching with multiple optical ring cavities. *Appl. Opt.* **41**, 6360–6370 (2002)
34. F. Beyrau, M.C. Weikl, T. Seeger, A. Leipertz, Application of an optical pulse stretcher to coherent anti-stokes Raman spectroscopy. *Opt. Lett.* **29**, 2381–2383 (2004)